The Astrophysical Journal, 563:462–471, 2001 December 10

LABORATORY MEASUREMENTS OF IRON L-SHELL EMISSION: 3→2 TRANSITIONS OF Fe XXI–XXIV BETWEEN 10.5 AND 12.5 Å

M. F. Gu,[1] S. M. Kahn, D. W. Savin, and E. Behar
Department of Physics and Columbia Astrophysics Laboratory, Columbia University, New York, NY 10027
and
P. Beiersdorfer, G. V. Brown, D. A. Liedahl, and K. J. Reed
Department of Physics and Space Technology, Lawrence Livermore National Laboratory, Livermore, CA 94550
Received 2001 January 10; accepted 2001 August 8

ABSTRACT

Using the electron beam ion trap EBIT-II facility at Lawrence Livermore National Laboratory, we have measured the iron L-shell spectrum between 10.5 and 12.5 Å for Fe XXI–XXIV with a spectral resolution of ~30 mÅ. The relative line intensities of strong 3 → 2 transitions for each charge state are measured as functions of electron energy and compared to distorted wave (DW) calculations. The contributions of resonant processes, namely, resonant excitation (RE) and spectroscopically unresolved dielectronic recombination (DR) satellites, are investigated. The RE contributions are shown to be less than the experimental and theoretical uncertainties for plasma in collisional ionization equilibrium. The unresolved DR satellites, however, enhance the emissivities of almost all lines, some by as large as 15%, consistent with our earlier measurements for Fe XXIV. The DW results agree with our measurements to better than 20% under the condition of collisional ionization equilibrium. The line emissivities in the widely used spectral synthesis model, MEKAL, are also compared to our measurements and are found to be discrepant at a greater than 20% level for some lines.

Subject headings: atomic data — atomic processes — line: formation — X-rays: general

1. INTRODUCTION

The diagnostic importance of iron L-shell transitions has been emphasized many times in the literature (Kahn & Liedahl 1990). The richness of the iron L-shell spectrum and the high cosmic abundance of iron make these among the most prominent discrete features in the X-ray spectra of a wide variety of cosmic sources. However, until recently, it has been very difficult to make full diagnostic use of iron L-shell emission lines in astrophysical X-ray spectra because of the inadequate spectral resolution of most available measurements and the insufficient understanding and inclusion of the atomic physics responsible for the line excitations in spectral synthesis models. With the launches of *Chandra* and *XMM-Newton*, the first problem has been largely overcome. The second problem, however, still introduces uncertainties in spectral modeling, thereby precluding reliable interpretation of the data.

Generally, analyses of X-ray spectra from extrasolar sources have relied on spectral synthesis codes. Among these, RS (Raymond & Smith 1977), MEKA, and its updated version MEKAL (Mewe, Kaastra, & Liedahl 1995) are the most widely used. Even with the moderate resolution of *ASCA*, several observations have shown discrepancies with the atomic data contained in these codes (Fabian et al. 1994). It is clear that more accurate and complete information about line excitation rates and wavelengths need to be incorporated.

Several approaches can be taken to accomplish this goal. Extensive theoretical calculations have proven to be valuable in providing the large amount of data needed to improve the spectral modeling. For example, the incorporation of the distorted wave (DW) calculations using the Hebrew University Lawrence Livermore Atomic Code (HULLAC) into the MEKA code resulted in the new version MEKAL, which provided better agreement with *ASCA* observations in the spectral region dominated by the iron L-shell complex (Liedahl, Osterheld, & Goldstein 1995). However, for high-Z multielectron systems like iron L-shell ions, it is very difficult to assess the accuracy of any theoretical calculations. One must rely on experimental measurements for benchmarking these codes. Several such experimental investigations have been performed in recent years to calibrate the wavelengths and intensities of iron L spectral lines using both laboratory sources and solar X-ray spectra (Brown et al. 1998; Phillips et al. 1999). Our group has been engaged in a systematic effort to measure excitation cross sections for iron L-shell transitions using the Lawrence Livermore electron beam ion trap EBIT-II. Among available laboratory plasma sources, the electron beam ion trap is unique in that it provides the capability to produce highly charged ions under well-controlled conditions and to isolate different line formation processes for individual study. Using the EBIT-II device, Brown et al. (1998) measured the wavelengths of Fe XVII line emission in the 9.8–17.5 Å range, and a thorough survey in the 10.6–18.0 Å range for all significant emission from Fe XVIII–XIV has been presented by Brown et al. (1999a). Savin et al. (1996) measured the line ratios of several Fe XXIV 3 → 2 and 4 → 2 transitions at electron energies far beyond the excitation thresholds, supporting the DW calculations of HULLAC and Zhang, Sampson, & Clark (1990). Gu et al. (1999a) extended the Fe XXIV measurements to the near-threshold region, where resonant processes are important, namely, dielectronic recombination (DR) and resonant excitation (RE). DR produces spectroscopically unresolved satellite lines when the captured electron is in the high-lying Rydberg levels. In RE, the resonance state formed through dielectronic capture autoionizes to an excited state, which

[1] Chandra Fellow at Center for Space Research, Massachusetts Institute of Technology, Cambridge, MA 02139.

may then radiatively decay to form spectral lines. These processes are described in more detail in Gu et al. (1999a).

In the work of Gu et al. (1999a), it was shown that, for plasma in collisional ionization equilibrium, DR satellites with the captured electron in the $n \geq 5$ levels (n is the principal quantum number) can enhance the emissivity by $\sim 10\%$ for the three principal transitions from Fe XXIV studied and that the RE contributions are not significant. One drawback of those measurements was that the electron beam energy extended only up to 3.0 keV. In order to determine the relative contributions of resonant processes to the rate coefficients, we had to use HULLAC calculations for excitation cross sections at electron energies beyond 3.0 keV. Although our measurement showed excellent agreement with the HULLAC results for electron energies between 2.0 and 3.0 keV, where resonant processes do not play a role, it is not clear that this will also be the case for other transitions. We therefore have carried out new measurements using the same technique, except that the maximum electron energy is ~ 8.0 keV, i.e., up to 8 times the threshold energy for excitation. The three Fe XXIV lines studied in our previous work are relatively free of blending and allowed us to use simple fitting procedures to extract the relevant line intensities. However, the majority of the iron L-shell lines for lower charge states are in crowded spectral regions. In this paper, we develop a more sophisticated analysis technique to infer the line intensities of all relatively strong lines in the wavelength range we covered. Using this new method, we reanalyze the near-threshold data in the previous experiment. Combining these with the new data at higher energies, we examine the accuracy of DW calculation for strong emission lines from Fe XXI–XXIV and the contributions of resonant processes.

This paper is structured as follows: After a brief review of the experimental technique in § 2, we describe our data analysis procedure in detail in § 3. The results are presented in § 4. Finally, we summarize and give conclusions in § 5.

2. EXPERIMENTAL TECHNIQUE

The Livermore electron beam ion trap (Levine et al. 1988) incorporates a magnetically confined electron beam, which produces a potential well that traps positively charged ions in the radial direction. In the axial direction, ions are trapped electrostatically by a positive bias applied to top and bottom drift tubes. The electron beam also ionizes and excites the trapped ions. The X-ray emission from the trap region is measured with flat crystal spectrometers (Beiersdorfer & Wargelin 1994; Beiersdorfer et al. 1997; Brown, Beiersdorfer, & Widmann 1999b). In the experiments we describe here, thallium acid phthalate crystals with $2d$ spacing of 25.76 Å were used. The diffracted X-rays were detected by position-sensitive proportional counters (PSPCs) at a direction perpendicular to the electron beam. The lengths of the crystal and the PSPC window restrict the wavelength coverage to within 10.5–12.5 Å, which contains almost all $3 \rightarrow 2$ lines of Fe XXIII and XXIV and some of the strongest of Fe XXI and XXII.

We used the same electron beam energy sweeping technique as in the near-threshold measurement (Gu et al. 1999a), but with a much larger energy range, ~ 0.75–8.0 keV. The timing pattern for the sweep is shown in Figure 1. The ionization and recombination timescales are much longer than the time spent to sweep the beam energy. Therefore, the charge balance changes insignificantly during the cycle. By varying the beam current synchronously with the beam energy, we were able to maintain a constant electron density. The independence of ion abundance and electron density on the beam energy allow the energy dependence of the emission rate of any line to be mapped out. The relative intensities of lines from the same charge state could also be determined given our knowledge of the spectrometer efficiency as a function of wavelength.

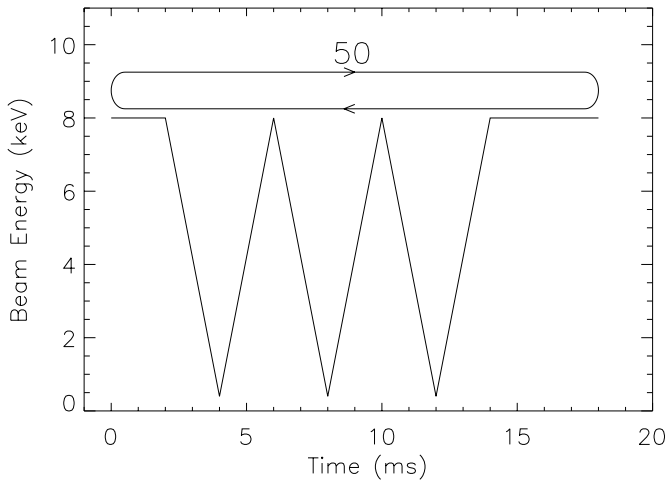

FIG. 1.—Timing pattern used to sweep the electron energy. The time spent ramping is 12 ms out of an 18 ms loop.

3. DATA ANALYSIS

An event-mode data acquisition system was used to collect the data (Knapp et al. 1993). The time of the detection, the wavelength of the photon, and the beam energy as indicated by the high-voltage (HV) monitor of the power supply are recorded for each event. The HV monitor, however, was not suitable for indicating the electron energy because of the inherent noise and the delay of the HV actually being applied to the drift tubes relative to the monitor. Instead, we used the time of the photon detection to infer the beam energy according to the timing pattern of the sweep. In Figure 2, a scatter plot of the data in the E-λ plane is shown, where E is the electron energy and λ is the photon wavelength. The total spectrum summed over all electron energies is also shown in Figure 2 with the identified lines, for which the line intensities were measured.

3.1. *Model of the Spectrometer Response*

For each time interval, or equivalently, electron energy interval, we construct a spectral model for comparison with the data via the equation

$$C_n = \sum_i S_i A_q G_i(E) \varepsilon(\lambda_i) R(n - n_i) + b_n , \qquad (1)$$

where C_n is the number of photon counts within the spectral channel n, A_q is the product of ion abundance, beam density, and beam-ion overlap, $G_i(E)$ is an intensity correction factor at beam energy E due to the polarization and anisotropy of the radiation (see below), b_n is the background, and the sum is taken over all spectral lines with line intensities S_i that are expected to contribute to the spectrum. The functions ε and $R(n - n_i)$ are the efficiency and line redistribution function (LRF) of the crystal spectrometer, where n_i is the line center expressed in the channel position.

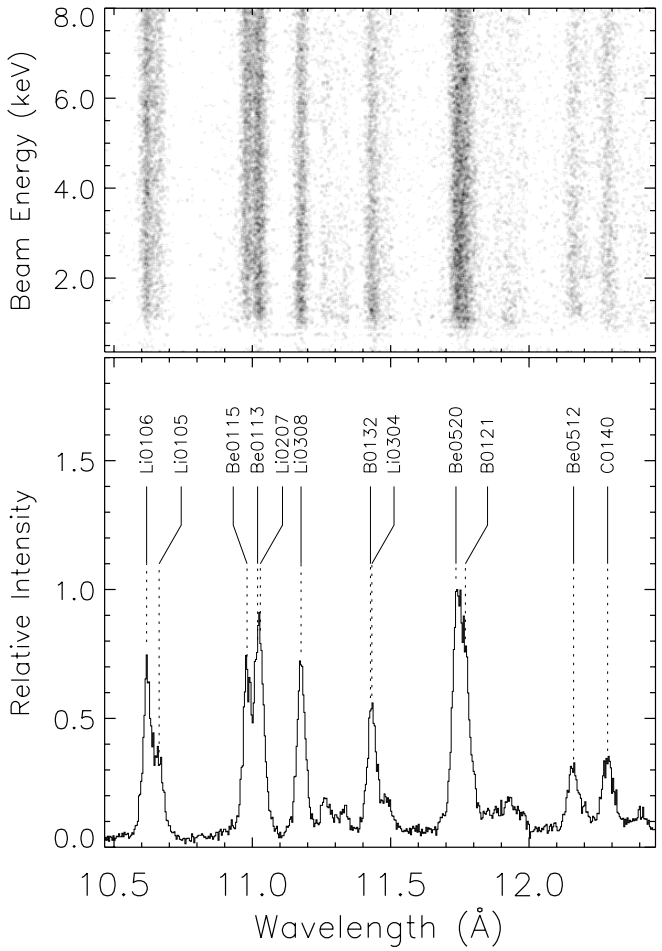

FIG. 2.—Scatter plot and total spectrum. Each point in the top panel represents a photon. The x-axis is the photon wavelength, and the y-axis is the electron beam energy. Summing the photon counts over the beam energy produces the spectrum shown in the lower panel. The line labels are constructed with the isoelectronic notation of charge states followed by the energy-level indexes of the lower and upper levels. For wavelengths and the configurations of the lower and upper levels, see Table 3.

The line center as a function of the Bragg angle is approximately linear. The deviation from linearity, however, is substantial in the 2 Å wavelength range covered by our measurements. Even a quadratic approximation is found to be inadequate. We therefore model it as a third-order polynomial,

$$n_i = a_0 + a_1\,\theta_i + a_2\,\theta_i^2 + a_3\,\theta_i^3\ , \tag{2}$$

where θ_i is the Bragg angle determined by $2d\ \sin\ \theta_i = \lambda_i$.

The efficiency $\epsilon(\lambda)$ is determined by the various window transmission functions, the quantum efficiency of the PSPC, and the crystal reflectivity. Using the atomic scattering factors of Henke et al. (1993), these contributions are calculated and used in the spectral analysis.

The LRF of the crystal spectrometer can be approximated accurately by a Voigt profile, which is the convolution of a Gaussian and a Lorentzian. If the FWHMs of the Lorentzian and Gaussian components are $w_{\rm L}$ and $w_{\rm G}$, respectively, the normalized Voigt function is

$$V(w_{\rm L},\, w_{\rm G},\, x) = \frac{1}{\pi^{3/2}}\,\frac{a}{\Delta}\int_{-\infty}^{+\infty}\frac{\exp\,(-y^2)dy}{a^2 + (u-y)^2}\ , \tag{3}$$

where

$$\Delta = \frac{w_{\rm G}}{2\sqrt{\ln 2}}\ ,$$

$$a = \frac{w_{\rm L}}{2\Delta}\ ,$$

$$u = \frac{x}{\Delta}\ . \tag{4}$$

Highly accurate numerical methods for the calculation of the Voigt function are given in Armstrong (1967) and Drayson (1976). These procedures are rather complicated. For spectral fitting, a simpler method has been adopted. This involves a linear mixing of Lorentzian and Gaussian functions to form a simple analytical representation of the Voigt profile (Henke et al. 1978):

$$\tilde{V}(\delta,\, w_v,\, x) = \delta G(t) + (1-\delta)L(t)\ , \tag{5}$$

where $t = 2x/w_v$ with w_v being FWHM of the Voigt function; $G(t)$ and $L(t)$ are Gaussian and Lorentzian functions with unit height

$$G(t) = \ \exp\,(-t^2 \ln 2)\ ,$$

$$L(t) = \frac{1}{1+t^2}\ . \tag{6}$$

In this approximation, the original parameters characterizing the Voigt function, $w_{\rm L}$ and $w_{\rm G}$, are replaced with δ and w_v. The term δ is referred to as the Gaussian fraction and ranges between zero for a pure Lorentzian and unity for a pure Gaussian. From the measured spectra, we notice that taking δ as a constant across the entire wavelength range is a good approximation, while w_v shows considerable variation. We model w_v as a linear function of the Bragg angle in our analysis:

$$w_v = w_0 + w_1\,\theta_i\ . \tag{7}$$

There are seven parameters in total that determine the line redistribution function. In the current experiment, we have taken a spectrum with the H-like and He-like lines of Ne, which fall within the desired wavelength range to calibrate the wavelength scale and determine the parameters in the line redistribution function. Since this Ne spectrum is much simpler, we fit it to derive the parameters in the LRF. For the near-threshold data, no calibration spectrum was taken; we derived these parameters directly from the data. The background term b_n is assumed to be linear in the Bragg angle. This assumption appears to be adequate for the wavelength range observed here.

The correction factor $G(E)$ is due to the polarization and anisotropy of the radiation. This factor arises because the directional electron beam populates the magnetic sublevels differently. For transitions that can be approximated by a single multipole operator,

$$G(E) = \left(1 + \frac{1-P}{1+P}f\right)\sum_{\lambda\,=\,\rm even} g_\lambda\,A_\lambda\,B_\lambda\ , \tag{8}$$

where $f = R_\pi/R_\sigma$; R_π and R_σ are the integrated reflectivities of the crystal for radiation polarized along the dispersion plane and perpendicular to the dispersion plane; A_λ are angular distribution coefficients, which depend only on the angular momentums of the lower and upper levels of the

TABLE 1

LINE REDISTRIBUTION FUNCTION PARAMETERS FOR BOTH LOW-ENERGY AND HIGH-ENERGY DATA

Parameter	Low Energy	High Energy
a_0	1235.7	1043.2
a_1	16125	17524
a_2	−9004.8	−3244.3
a_3	−169229	−44550
w_0	23.6	24.6
w_1	80.2	132.7

NOTES.—Parameters a_0–a_4 are for wavelength scale. Parameters w_0 and w_1 are for line widths.

transition; B_λ are the orientation parameters, which are determined by the population of the magnetic sublevels; g_λ account for the fact that the electron beam is not strictly unidirectional (Gu, Savin, & Beiersdorfer 1999b); and P is the polarization parameter, defined as

$$P = \frac{I_\sigma - I_\pi}{I_\sigma + I_\pi}, \tag{9}$$

where I_π and I_σ are the intensities of emitted radiation polarized along the dispersion plane and perpendicular to the dispersion plane (Percival & Seaton 1958). It can also be expressed in terms of g_λ, A_λ, and B_λ as described in Gu et al. (1999b). In our analyses, the direct excitation cross section to the different magnetic sublevels were calculated using the relativistic DW code of Zhang et al. (1990). The populations due to cascades were neglected. In general, the correction factors $G(E)$ for polarized lines are $\lesssim$10%–20%.

3.2. *Normalization*

The parameters A_q involve the abundance of each ion, the electron density, and the beam-ion overlap factor. Although their exact values are not known, our experimental technique ensures that they do not depend on the beam energy. The electron energy independence of these factors is the key element of our measurement. The validity of this condition has been verified by measuring radiative recombination emission in a similar experimental setting (Savin et al. 2000). Fixing these values provides a normalization level for the lines of each ion. To accomplish this, we choose a beam energy region where theoretical cross sections are known to be accurate. The observed spectra in that energy band are then fitted by fixing the sum of the intensities of all strong lines for each charge state according to the theoretical calculations and leaving the A_q as free parameters. The A_q parameters obtained in the fitting are then used in the spectral fits at individual beam energies, where the excitation cross sections are much more uncertain. Therefore, the normalization is carried out for each charge state rather than individual lines. It ensures that in a suitable high-energy region, the experimental sum of the intensities of all strong lines from each charge state matches the corresponding theoretical sum.

TABLE 2

ION ABUNDANCE PARAMETERS A_q FOR BOTH LOW-ENERGY AND HIGH-ENERGY DATA

Charge State	Low Energy	High Energy
Fe XXIV.....	38854	4633.0
Fe XXIII.....	32294	2375.8
Fe XXII	21219	1341.8
Fe XXI	3516.7	319.78

3.3. *Spectral Fitting Method*

The simple line-fitting method used in Gu et al. (1999a) for Fe XXIV is insufficient for lower charge states, where each ion contributes hundreds of weak lines in a narrow wavelength band. Even with a resolving power of 500, these weak lines form a pseudocontinuum. Moreover, many strong lines sitting above this pseudocontinuum are blends of two or more components, which often originate from different charge states. Fortunately, for each charge state, the number of lines that provide the most important diagnostic information is not large. Nevertheless, the pseudocontinuum formed by the weak lines represents a considerable fraction of the total line power and cannot be completely neglected. One practical procedure is to construct a theoretical model for these weak emission lines while leaving the strong-line intensities as free parameters to be determined by the experiment. When two or more strong lines are blended, it is not possible to derive individual line parameters without ambiguity. In such cases, we fix the ratio of the emissivity of these lines based on the theoretical model.

The wavelengths of many strong iron L-shell lines have been accurately measured in the laboratory (Brown et al. 1999a) and with solar observations (Phillips et al. 1999). At the resolution of the EBIT-II crystal spectrometers, they can often be fixed at these known values in the spectral fitting. When the line redistribution function is known from the calibration spectra, the free parameters S_i enter the spectral model linearly. Linear least-squares methods are very efficient for such spectral fitting problems. However, to incorporate the constraints imposed on blended lines and the nonnegative nature of emission-line intensities in the fitting procedure, the standard linear least-squares algorithms are not suitable. We therefore recast the linear least-squares problem into a quadratic programming (QP) problem and used general constrained QP algorithms to find the best-fitting line intensities. The high efficiency of such algorithms enabled us to carry out Monte Carlo simulations to determine the statistical errors in the derived line intensities, which are more reliable than those obtained through a covariance matrix calculated at the fitted model.

Occasionally, wavelengths of some lines had to be determined from the data along with the intensities, and for the near-threshold data, the LRF parameters had to be derived from the data directly. In these cases, the fitting becomes a general nonlinear least-squares problem. Although the Levernberg-Marquart algorithm can be used in the spectral fitting, it ignores the fact that most free parameters enter the model linearly. To take advantage of this property, we use a variable projection method in solving such nonlinear least-squares problems. The mathematical details of this method can be found in Kaufman & Pereyra (1978). Here we outline only the general idea of the algorithm. The spectral fitting problem at hand is equivalent to minimizing the functional

$$r(\boldsymbol{a}, \alpha) = \sum_i [y_i - \sum_j a_j \phi_j^i(\alpha)]^2 , \tag{10}$$

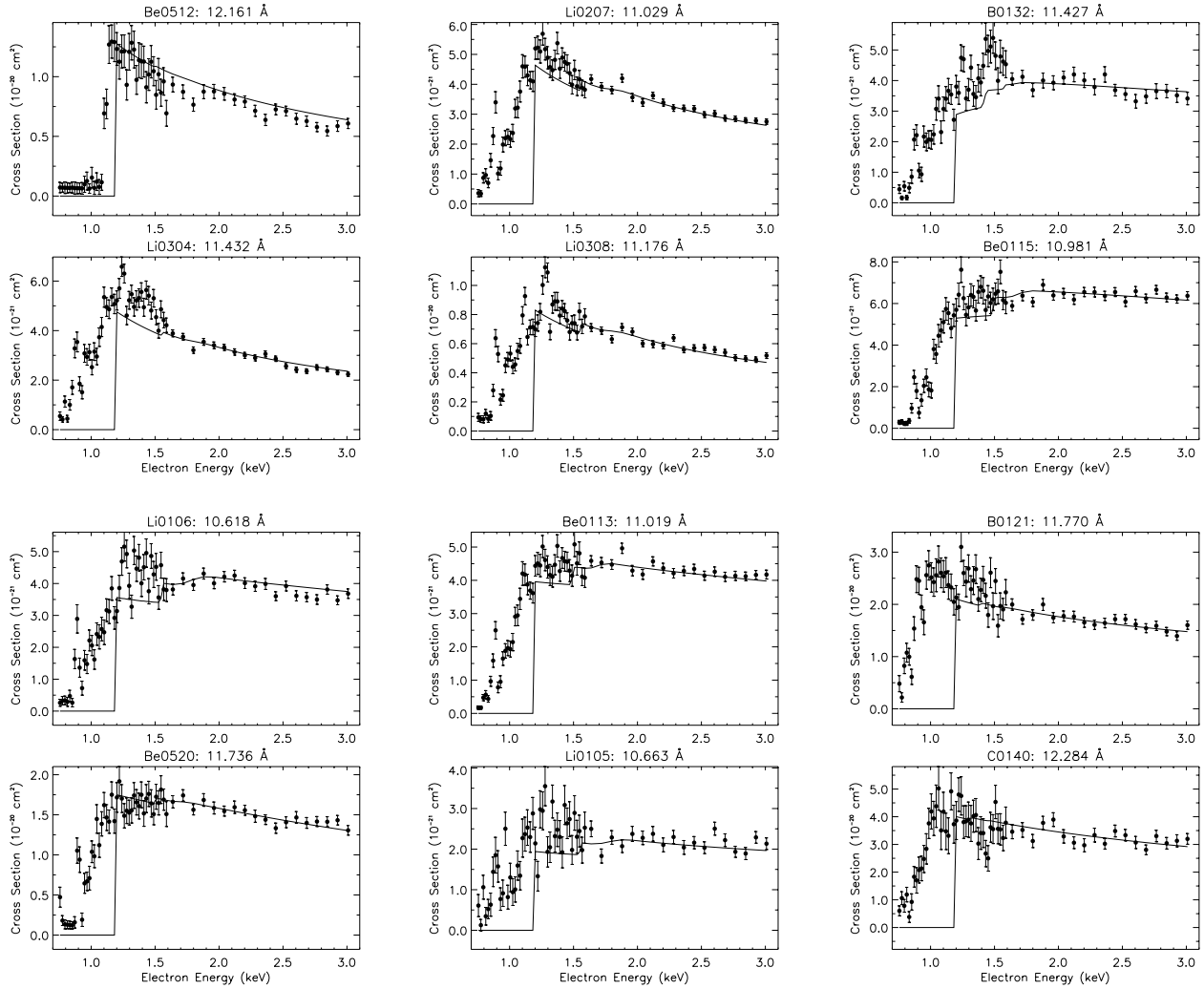

FIG. 3.—Cross sections for the formation of $3 \rightarrow 2$ lines from the near-threshold data. The error bars represent 1 σ statistical uncertainties. The solid lines are HULLAC calculations for DE only.

where α is a vector representing nonlinear parameters such as wavelengths and $\boldsymbol{a}$ represents linear parameters such as line intensities. If we define a matrix Φ whose elements are $\Phi_{ij} = \phi_j^i$, the above functional can be written as

$$r(\boldsymbol{a}, \alpha) = \| \boldsymbol{y} - \Phi(\alpha)\boldsymbol{a} \|^2 . \quad (11)$$

The key idea of the variable projection method is to reduce the above minimization to two subproblems. The first subproblem is a nonlinear least-squares problem in the variable α and involves finding that α which minimizes

$$r_2(\alpha) = \| \boldsymbol{y} - \Phi(\alpha)\Phi^{\dagger}(\alpha)\boldsymbol{y} \|^2 , \quad (12)$$

where $\Phi^{\dagger}$ denotes the pseudoinverse of Φ as described by Rao & Mitra (1971). The second subproblem is simply a linear least-squares problem of finding $\boldsymbol{a}$ that minimizes

$$\| \boldsymbol{y} - \Phi(\hat{\alpha})\boldsymbol{a} \|^2 , \quad (13)$$

where $\hat{\alpha}$ is the solution of the first subproblem. The variable projection method is most suitable when the number of linear parameters is much larger than the number of nonlinear parameters. This is the situation in our spectral analysis, since the number of line intensities to be determined always exceeds the number of unknown wavelengths.

After the detected photons are binned in both wavelength and electron energy, we use the method described above to fit the spectrum at different electron energies. The resulting line intensities reflect the energy dependence of the excitation cross sections.

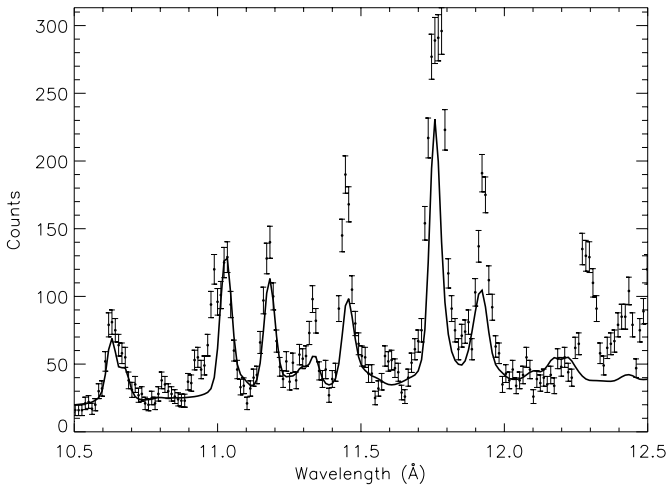

FIG. 4.—Solid line is the theoretical spectrum of DR $3l5l'$ and $3l6l'$ DR satellites of Fe XXII–XXIV calculated with HULLAC. The data points are the measured spectrum with electron energy between 0.8 and 1.0 keV.

TABLE 3

MEASURED $3 \rightarrow 2$ LINES FROM Fe XXI–XXIV

Number	Label	Label[a]	Upper	J	Lower	J	λ^b (Å)	λ^c (Å)
1	Li0106	...	$1s^2 3p_{3/2}$	$\frac{3}{2}$	$1s^2 2s$	$\frac{1}{2}$	10.618	10.620
2	Li0105	Li5	$1s^2 3p_{1/2}$	$\frac{1}{2}$	$1s^2 2s$	$\frac{1}{2}$	10.663	10.663
3†	Li0207	Li4	$1s^2 3d_{3/2}$	$\frac{3}{2}$	$1s^2 2p_{1/2}$	$\frac{1}{2}$	11.029	11.034
4	Li0308	Li3	$1s^2 3d_{5/2}$	$\frac{5}{2}$	$1s^2 2p_{3/2}$	$\frac{3}{2}$	11.176	11.178
5‡	Li0304	Li1	$1s^2 3s$	$\frac{1}{2}$	$1s^2 2p_{3/2}$	$\frac{3}{2}$	11.432	11.433
6	Be0115	Be9	$1s^2 2s 3p_{3/2}$	1	$1s^2 2s^2$	0	10.981	10.983
7†	Be0113	Be8	$1s^2 2s 3p_{1/2}$	1	$1s^2 2s^2$	0	11.019	11.021
8	Be0520	Be2	$1s^2 2s 3d_{5/2}$	2	$1s^2 2s 2p_{3/2}$	1	11.736	11.763
9	Be0512	Be1	$1s^2 2s 3s$	0	$1s^2 2s 2p_{3/2}$	1	12.161	12.187
10‡	B0132	B19	$1s^2 2s^2 2p_{3/2} 3p_{3/2}$	$\frac{3}{2}$	$1s^2 2s^2 2p_{1/2}$	$\frac{1}{2}$	11.427	11.435
11	B0121	B13	$1s^2 2s^2 3d_{3/2}$	$\frac{3}{2}$	$1s^2 2s^2 2p_{1/2}$	$\frac{1}{2}$	11.770	11.782
12	C0140	C10	$1s^2 2s^2 2p_{1/2} 3d_{3/2}$	1	$1s^2 2s^2 2p_{1/2}^2$	0	12.284	11.292

NOTE.—The intensities of lines marked with a dagger (†) or double dagger (‡) are linked in the fitting.

[a] Label of Brown et al. 1999a.

[b] Measured by Brown et al. 1999a.

[c] HULLAC.

4. RESULTS

4.1. *Reanalysis of the Near-Threshold Data*

The near-threshold data reported in Gu et al. (1999a) are reanalyzed with the method discussed in the last section. A normalization spectrum is first generated by summing the line emission at electron energies between 2.0 and 3.0 keV. This spectrum is fitted to determine the LRF and parameters A_q that fix the normalization level. These parameters are listed in Tables 1 and 2. In the fitting of normalization spectra, wavelengths that have been measured by Brown et al. (1999a) are fixed at their experimental values. Both intensities and wavelengths of lines that are weaker than 5% of the strongest line in the spectrum are fixed according to theory. Since no calibration spectra were taken in this run, the LRF parameters are left as free parameters. Only lines from Fe XXI–XXIV have appreciable flux; we therefore include only these ions in the spectral model. In Table 3, we show all $3 \rightarrow 2$ lines from Fe XXI–XXIV that are strong enough for the intensities to be derived meaningfully. The line labels are constructed with the isoelectronic notation of the ion followed by the energy-level indexes of the lower (first two digits) and upper (remaining digits) levels as calculated by HULLAC. Note that some level designations may be in a different order in other theoretical calculations because of the uncertainties in the calculated level energies. The measured wavelengths from Brown et al. (1999a) and the theoretical wavelengths from HULLAC are listed. The corresponding line labels given in Brown et al. (1999a) and the relativistic configurations of the lower and upper levels are also given. Some of the lines are unresolved. In such cases, we fix the relative intensity of these lines according to theory. The links between these lines are also indicated in Table 3.

Data are binned in beam energy. Below 1.6 keV, where resonances are expected, the energy width of each bin is ~ 20 eV. Above 1.6 keV, it is ~ 80 eV, since the cross sections should be quite smooth. The spectrum at each beam energy is fitted separately using LRF parameters and A_q as derived from the normalization spectra. The fitted line intensities at individual energy bins are therefore relative to the theoretical calculations in the normalization energy region for each charge state. The cross sections derived from the fitted line intensities are an average in the sense that

$$\bar{\sigma} = \frac{1}{\int_{\Delta E} G(E) v \, dE} \int_{\Delta E} G(E) \sigma v \, dE \, , \tag{14}$$

where the integration is over each energy bin. With such a small bin size, the cross sections and intensity correction factors do not change significantly within one bin. This average cross section is essentially the same as the cross section at the bin center. In Figure 3, the cross sections as functions of beam energy are shown and compared with HULLAC calculations. These calculations include direct excitation from the ground state by electron impact and radiative cascades within the $n = 3$–7 complex. Collisional excitation from excited levels are neglected, since for these processes to be important in the relevant ions, the electron density has to be greater than 10^{13} cm^{-3} (Kahn & Liedahl 1990), while in our experiment, the effective electron density taking into account the beam-ion overlap is less than 10^{12} cm^{-3}. The calculations do not include resonance effects either. The error bars on data points show the statistical uncertainties quoted at a 1 σ confidence level and are determined by Monte Carlo simulations.

RE effects can be seen at energies just above excitation threshold for almost all lines studied. They are produced by resonant dielectronic capture followed by Auger emission into an excited state, which decays by $3 \rightarrow 2$ photon emission. Because these are not included in the HULLAC calculations used, Gu et al. (1999a) compared these effects on three Fe XXIV lines with detailed $\boldsymbol{R}$-matrix calculations. They pointed out that to delineate these resonances, the energy grid in the computation has to be extremely dense. We are unaware of any similar calculations of $n = 2 \rightarrow 3$ excitation processes for other iron L-shell ions. We discuss the RE contributions to the rate coefficients for thermal plasma in § 4.3, based on our measurements.

Below the excitation threshold, each line shows DR satellite emission that is spectroscopically unresolved. The lowest electron energy in our experiments is ~ 0.75 keV; therefore, the data include only resonances of the type $3lnl'$ with $n > 4$. Using HULLAC, the DR satellite spectra associated with the $3lnl'$ resonances with $n = 4$, 5, and 6 have been calculated for Fe XXII–XXIV. For $n = 5$ and 6, the shifts in satellite wavelengths relative to the main lines are

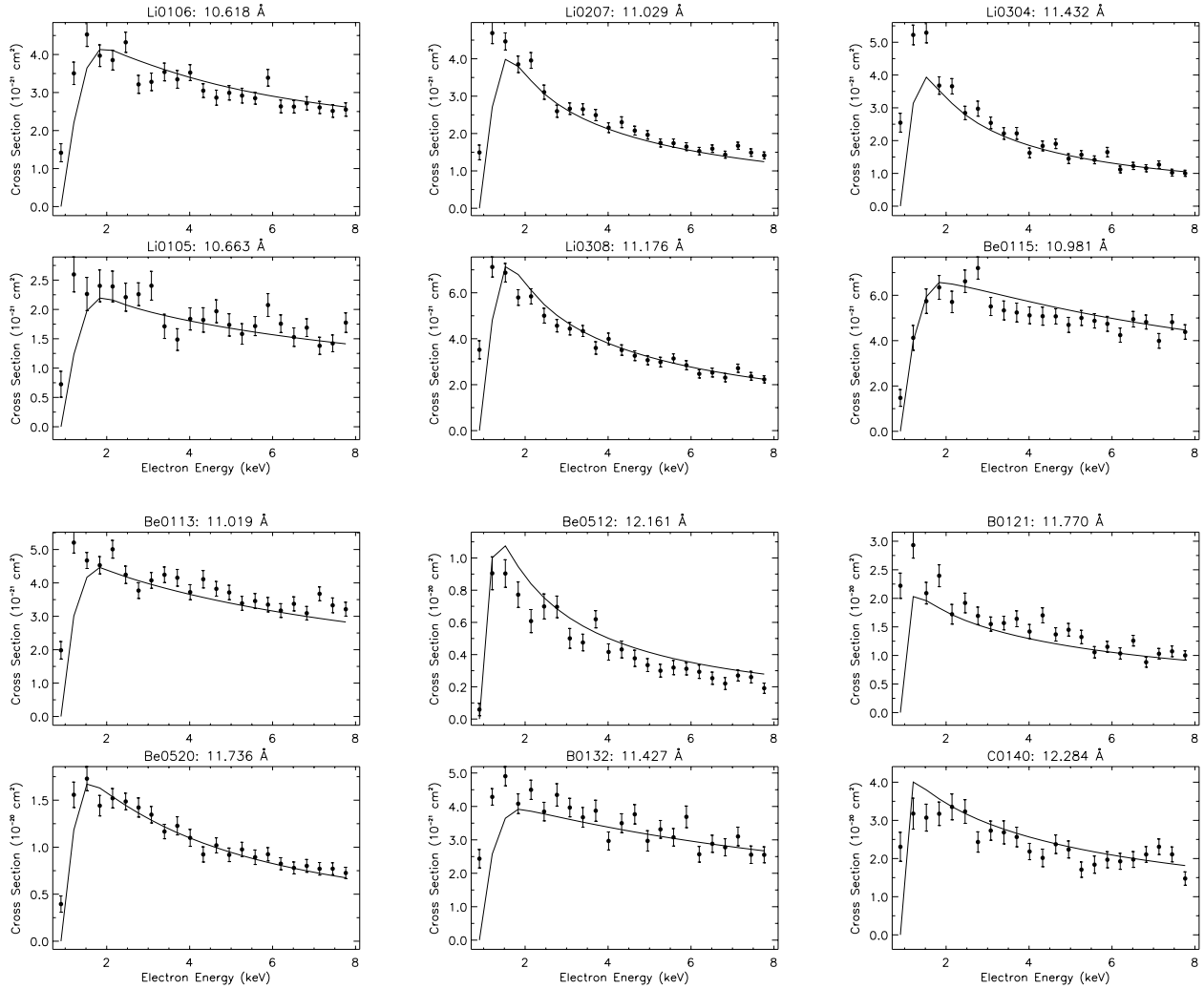

FIG. 5.—Cross sections for the formation of $3 \rightarrow 2$ lines from the high-energy data. The error bars represent 1 σ statistical uncertainties. The solid lines are the HULLAC calculations.

difficult to detect at our spectral resolution; their values are therefore fixed in the spectral fitting. Using the known ion abundance parameters A_q, we can directly compare the theoretical satellite spectra with our measurements. However, due to the beam energy spread, DR resonances for $n = 5$ and 6 partially overlap, especially for Fe XXII, whose $3l6l'$ resonances are located at energies similar to those at the $3l5l'$ resonances of Fe XXIII and XXIV. The energy of the $3l7l'$ resonances can be estimated with the hydrogenic formula

$$E_r = \Delta E - \frac{z^2}{7^2} E_{\rm H} , \qquad (15)$$

where z is the effective charge of the recombining ion, ΔE is the excitation energy of the $3 \rightarrow 2$ transitions, and $E_{\rm H}$ is the ionization energy of hydrogen. For $3 \rightarrow 2$ transitions from Fe XXII through Fe XXIV, $\Delta E \sim 1.1$–1.2 keV; therefore, $E_r \gtrsim 1.0$ keV for the $n = 7$ resonances. If we sum the data for beam energies within 0.8–1.0 keV, the resulting spectrum should be primarily due to the $3l5l'$ and $3l6l'$ DR satellites. Figure 4 shows the experimental satellite spectra in this beam energy range compared with the calculations. The LRF parameters and A_q derived from the normalization energy region are used in constructing the theoretical satellite spectrum. The correction factors due to polarizations and anisotropy are not included in the calculated spectrum. These effects may change individual DR satellite line intensities by as much as a factor of 2 (Beiersdorfer et al. 1992). The average of many individual lines within a given resonance structure, however, is affected only by $\sim$10%–20% and converges to the correction of the parent line. Although the overall structure of the satellite spectrum is seen to match that of the data, there exist considerable quantitative discrepancies. Ignoring lines above 12.2 Å due to Fe XXI, which is not included in our calculation, theory seems to generally underestimate the satellite intensities.

According to our HULLAC calculations, the total flux of $3l4l'$ satellite lines comprises 36% of the combined $3lnl'$ flux with $n = 4$, 5, and 6 for Fe XXIII and Fe XXIV. For Fe XXII, this fraction is 39%. As can be seen in Figure 3, the intensities of DR satellite lines at collision energies above 1.0 keV are greater than those at lower energies. The total DR satellite flux at electron energies above 1.0 keV is at least as much as the $3l5l'$ and $3l6l'$ combined flux. Therefore, we estimate the contribution from the $3l4l'$ lines relative to the total DR satellites to be $\lesssim$25%. The $3l3l'$ satellite lines are even less important in collisionally ionized plasma, since these resonances occur at much lower energies, at $\sim$0.3 keV.

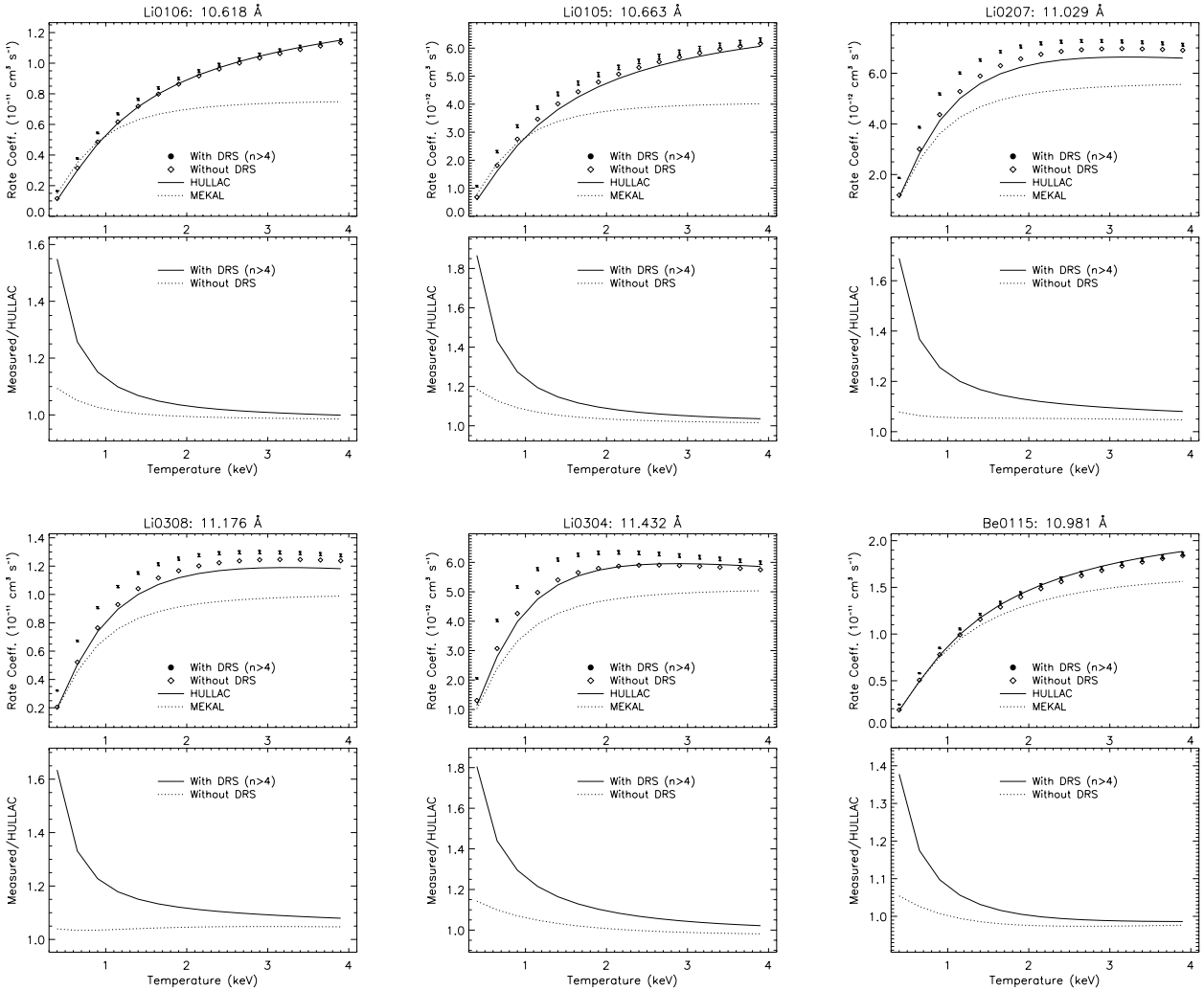

FIG. 6.—Rate coefficients for the formation of $3 \rightarrow 2$ lines. In the top panels, the HULLAC calculations and the rates from the MEKAL model are compared with our measurements. The open diamonds are the measurements without including DR satellite lines. The circles are the measurements with DR satellite lines. Error bars represent 1 σ statistical uncertainties. In the bottom panels, the ratios of the measured rate coefficients with and without DR satellite lines to the HULLAC rate coefficients are shown.

4.2. *High-Energy Data*

For collisionally ionized plasma, the temperatures where iron L-shell ion abundances peak are in the range of 0.5–2.0 keV. At such temperatures, the collisional excitation at energies above 3.0 keV contributes significantly to the total rate coefficients. Our high-energy data, which covers the energy up to 8.0 keV, was obtained to benchmark theory in this energy region.

The calibration spectrum was first analyzed, and the LRF parameters were determined. These parameters are then fixed at all subsequent spectral fittings. A normalization spectrum is generated from the data in the electron energy region of 2.0–8.0 keV. Fitting this normalization spectrum gives the ion abundance parameters A_q. Tables 1 and 2 list these parameters.

Since excitation cross sections at high energies are expected to be quite smooth, we chose the beam energy bin, 300 eV, to be larger than that in the near-threshold data. Figure 5 shows the average cross sections in the sense of equation (14) for the same $3 \rightarrow 2$ lines presented in the near-threshold data. Although the resonance structures at low energies do not show up because of the large energy bin, the discrepancy between the data and the calculations for DE shows clearly the effects of DR satellites at energies below the excitation thresholds. HULLAC calculations generally agree with the measurements for energies up to 8.0 keV.

4.3. *Rate Coefficients*

In thermal plasma, line emissivities are determined by rate coefficients, i.e., the integral of σv over the electron energy distribution. The near-threshold data have better statistics; we therefore use them in the calculation of this integral for emission at energies below 3.0 keV. The high-energy data are used for emission at 3.0–8.0 keV. For plasma at temperatures less than 2.0 keV, the contributions from emission above 8.0 keV are less than 10%. We use the HULLAC calculations to account for this and complete the integration. However, the near-threshold data and the high-energy data used different normalization energy regions. The discrepancy is not significant, as can be seen in the good agreement between the theory and measurements in the normalization energy region for both data sets. Never-

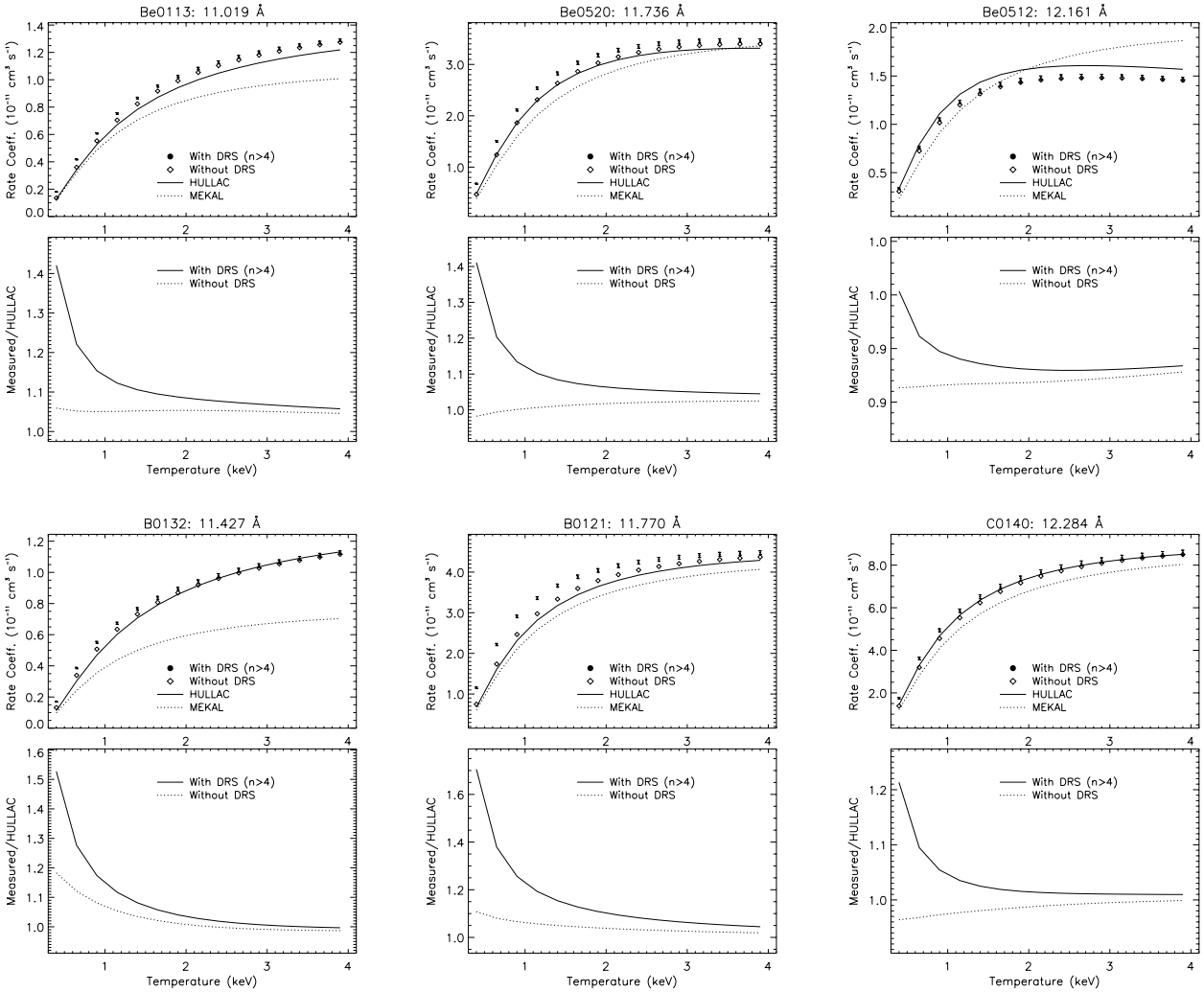

FIG. 6.—*Continued*

theless, we adjust the cross sections derived from both data sets slightly in such a way that they match each other in the energy region from 1.6 to 3.0 keV. In order to achieve this, we sum the high-energy data for beam energies between 1.6 and 3.0 keV and derive the line intensities. These intensities are compared with those derived from the near-threshold data in the same energy region. For each line, the average weighted by the statistical uncertainties is set to be the overall normalization; i.e., cross sections from both data sets are modified so that the line intensities in the 1.6–3.0 keV energy region are equal to these weighted averages.

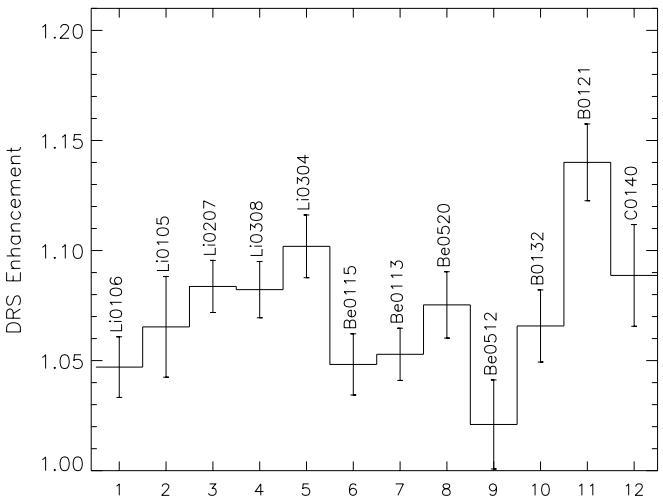

FIG. 7.—DR satellite enhancement for the twelve $3 \rightarrow 2$ lines studied here at temperatures where the abundance of the corresponding ions peaks in the collisionally ionized plasma. The figure shows the ratio of the measured rate coefficients with DR satellites to that without DR satellites.

Two rate coefficients, with and without DR satellites included, are derived for each line. In Figure 6, we compare these rate coefficients with HULLAC calculations and with the plasma model MEKAL. In the top panels, the measured rate coefficients with and without DR satellites are plotted together with the HULLAC and MEKAL rates. The bottom panels show the ratios of the measured rates over the HULLAC rates. The MEKAL rates are seen to deviate from both the HULLAC and measured rates significantly for most lines. The discrepancy between MEKAL and HULLAC rate coefficients is due to the fact that the excitation cross sections contained in the MEKAL model are a mixture of HULLAC results and the old MEKA model. The energy dependence of the cross sections used in MEKAL is the same as was used in MEKA. However, these cross sections have been partly updated by normalizing the MEKA cross sections to HULLAC results at an arbitrary energy. The differences between HULLAC and the measured rates without DR satellites are much smaller. This

indicates the overall accuracy of the DW approximation for these transitions. The small temperature dependence of the ratios of the measured rates without DR satellites to HULLAC shows that RE effects do not play an important role for plasma at temperatures greater than 0.5 keV. However, the contributions of the DR satellites are significant, especially at low temperatures. Figure 7 shows the ratios of the measured rates with and without DR satellites for each line at a temperature where the relevant ion abundance peaks according to the ionization balance of Arnaud & Raymond (1992). The enhancements due to DR satellites are seen to be as large as 15%. In one case, line Be0512, there is only a marginal contribution from DR satellites to the overall line intensity. The weakness of DR satellite emission for this line relative to DE is verified in theoretical calculations as shown in Figure 4.

5. CONCLUSIONS

We have measured the $3 \rightarrow 2$ line emission of Fe XXI–XXIV in the wavelength range of 10.5–12.5 Å. The cross sections for the excitation of 12 strong lines are measured at electron energies in the range 0.75–8.0 keV, and the Maxwellian-averaged rate coefficients are obtained as a function of temperature. These measurements are carried out in the low-density limit so that the excitation from excited levels can be neglected. The DW calculations are shown to agree well with our measurements at electron energies without resonances. The resonant processes at below or near excitation threshold energies, mostly DR satellites with the captured electron in $n > 4$ Rydberg levels, enhance the rate coefficients by as much as 15% depending on particular transitions involved. The calculated spectra of $3lnl'$ with $n = 4$, 5, and 6 show that the $n = 4$ satellites' flux is $\sim 40\%$ of the $n = 5$ and 6 combined flux. The wavelengths of the $n = 4$ satellites are, however, shifted with an amount detectable by the *Chandra* and *XMM-Newton* grating spectrometers.

We are delighted to thank Dan Nelson, Edward Magee, and Phil D'Antonio for their expert technical support. Work at the University of California Lawrence Livermore National Laboratory was performed under the auspices of the US Department of Energy under contract W-7405-ENG-48. This program was supported by NASA High Energy Astrophysics X-Ray Astronomy Research and Analysis grant NAGW-4185. The author (M. F. Gu) is currently supported by NASA through Chandra Postdoctoral Fellowship award PF01-10014 issued by the Chandra X-Ray Observatory Center, which is operated by the Smithsonian Astrophysical Observatory for and on behalf of NASA under contract NAS8-39073. D. W. Savin was supported in part by NASA Space Astrophysics Research and Analysis Program grant NAG5-5261 and NASA Solar Physics Research, Analysis, and Suborbital Program grant NAG5-9581.

REFERENCES

Armstrong, B. H. 1967, J. Quant. Spectrosc. Radiat. Transfer, 7, 61
Arnaud, M., & Raymond, J. 1992, ApJ, 398, 394
Beiersdorfer, P., Crespo López-Urrutia, J. R., Föster, E., Mahiri, J., & Widmann, K. 1997, Rev. Sci. Instrum., 68, 1077
Beiersdorfer, P., Phillips, T. W., Wong, K. L., Marrs, R. E., & Volgel, D. A. 1992, Phys. Rev. A, 46, 3812
Beiersdorfer, P., & Wargelin, B. J. 1994, Rev. Sci. Instrum., 65, 13
Brown, G. V., Beiersdorfer, P., Liedahl, D. A., Kahn, S. M., & Widmann, K. 1998, ApJ, 502, 1015
Brown, G. V., Beiersdorfer, P., Liedahl, D. A., Widmann, K., & Kahn, S. M. 1999a, Univ. California Lawrence Livermore National Laboratory Rep. No. UCRL-JC-136647
Brown, G. V., Beiersdorfer, P., & Widmann, K. 1999b, Rev. Sci. Instrum., 57, 1069
Drayson, S. R. 1976, J. Quant. Spectrosc. Radiat. Transfer, 16, 611
Fabian, A. C., et al. 1994, ApJ, 436, L63
Gu, M. F., et al. 1999a, ApJ, 518, 1002
Gu, M. F., Savin, D. W., & Beiersdorfer, P. 1999b, J. Phys. B, 32, 5371
Henke, B. L., Gullikson, E. M., & Davis, J. C. 1993, At. Data Nucl. Data Tables, 54, 181
Henke, B. L., Perera, R. C. C., Gullikson, E. M., & Schattenburg, M. L. 1978, J. Appl. Phys., 49, 480
Kahn, S. M., & Liedahl, D. A. 1990, in Iron Line Diagnostics in X-Ray Sources, ed. A. Treves, G. C. Perola, & L. Stella (Berlin: Springer), 3
Kaufman, L., & Pereyra, V. 1978, SIAM J. Numer. Anal., 15, 12
Knapp, D. A., Marrs, R. E., Schneider, M. B., Chen, M. H., Levine, M. A., & Lee, P. 1993, Phys. Rev. A, 47, 2039
Levine, M. A., et al. 1988, Phys. Scr., T22, 157
Liedahl, D. A., Osterheld, A. L., & Goldstein, W. H. 1995, ApJ, 438, L115
Mewe, R., Kaastra, J. S., & Liedahl, D. A. 1995, Legacy, 6, 16
Percival, I. C., & Seaton, M. J. 1958, Philos. Trans. R. Soc. London, A, 251, 113
Phillips, K. J. H., Mewe, R., Kaastra, J. S., Beiersdorfer, P., Brown, G. V., & Liedahl, D. A. 1999, A&AS, 138, 381
Rao, C. R., & Mitra, S. K. 1971, Generalized Inverse of Matrices and Its Applications (New York: Wiley)
Raymond, J. C., & Smith, B. W. 1977, ApJS, 35, 419
Savin, D. W., Beiersdorfer, P., Kahn, S. M., Beck, B. R., Brown, G. V., Gu, M. F., Liedahl, D. A., & Scofield, J. H. 2000, Rev. Sci. Instrum., 71, 3362
Savin, D. W., et al. 1996, ApJ, 470, L73
Zhang, H. L., Sampson, D. H., & Clark, R. E. H. 1990, Phys. Rev. A, 41, 198